Rong Yan
National NC System Engineering Research Center, Huazhong University of Science and Technology, Wuhan 430074, China
e-mail: yanrong@hust.edu.cn

Xiaowei Tang
National NC System Engineering Research Center, Huazhong University of Science and Technology, Wuhan 430074, China
e-mail: txwysxf@126.com

Fangyu Peng[1]
National NC System Engineering Research Center, Huazhong University of Science and Technology, Wuhan 430074, China;
State Key Laboratory of Digital Manufacturing Equipment and Technology, Huazhong University of Science and Technology, Wuhan 430074, China
e-mail: zwm8917@263.net

Yuting Li
National NC System Engineering Research Center, Huazhong University of Science and Technology, Wuhan 430074, China
e-mail: lytwhut@163.com

Hua Li
National NC System Engineering Research Center, Huazhong University of Science and Technology, Wuhan 430074, China
e-mail: M201570333@hust.edu.cn

RCSA-Based Method for Tool Frequency Response Function Identification Under Operational Conditions Without Using Noncontact Sensor

The stability lobe diagrams predicted using the tool frequency response function (FRF) at the idle state usually have discrepancies compared with the actual stability cutting boundary. These discrepancies can be attributed to the effect of spindle rotating on the tool FRFs which are difficult to measure at the rotating state. This paper proposes a new tool FRF identification method without using noncontact sensor for the rotating state of the spindle. In this method, the FRFs with impact applied on smooth rotating tool and vibration response tested on spindle head are measured for two tools of different lengths clamped in spindle–holder assembly. Based on those FRFs, an inverse receptance coupling substructure analysis (RCSA) algorithm is developed to identify the FRFs of spindle–holder–partial tool assembly. A finite-element modeling (FEM) simulation is performed to verify the validity of inverse RCSA algorithm. The tool point FRFs at the spindle rotating state are obtained by coupling the FRFs of the spindle–holder–partial tool and the other partial tool. The effects of spindle rotational speed on tool point FRFs are investigated. The cutting experiment demonstrates that this method can accurately identify the tool point FRFs and predict cutting stability region under spindle rotating state.
[DOI: 10.1115/1.4035418]

Keywords: tool FRFs, spindle rotating, inverse RCSA, chatter

1 Introduction

Chatter has significantly negative effect on productivity and quality guarantee of parts in machining applications. Stability analysis based on tool frequency response function (FRF) is a critical method to avoid chatter vibrations during cutting [1,2]. According to the stability lobe diagrams, the optimized cutting parameters, such as spindle speed and cutting depth, can be selected to improve material removal rate and surface finish.

The methods used to produce stability lobe diagrams require knowledge of the tool point FRFs which typically obtained using impact testing at the spindle idle state. However, the stability lobe diagrams predicted using the tool FRF at the idle state usually have discrepancies compared with the actual stability cutting boundary [3,4]. One major reason is the effect of the spindle rotating state on the tool point FRFs [3,5]. Because spindle rotating causes gyroscopic moments and centrifugal forces increasing, this then influences the dynamics of the spindle. In recent years, many scholars have proposed various methods to study the machine dynamics under operational conditions and demonstrated the speed-varying dynamics of spindles. Tounsi and Otho [6] obtained a pulselike cutting force on tool point by interrupted cutting of a narrow workpiece width and single tooth milling operations. Özsahin et al. [7] used the workpiece with random surface profile to produce random cutting forces. And the tool point–holder cross FRF is identified using the vibration response at the tool holder with a laser vibrometer. Similarly, Li et al. [8] and Cai et al. [9] studied the random excitation technique based on interrupted cutting of a narrow workpiece step while spindle rotating randomly. Zaghbani and Songmene [10] analyzed the spectrogram of the cutting force and the acceleration signal of the nonrotative part of the spindle on the spindle accelerating period and obtained the modal parameters by operational modal analysis during cutting. The cutting force excitation is limited by bandwidth, especially when the spindle is rotating at high speeds and the tool has multiteeth.

In addition to the direct excitation with cutting forces, noncontact excitation and measurement methods also have been studied. Mohanty and Risen [11] used the sinusoidal harmonic frequency

[1]Corresponding author.

Manuscript received August 29, 2016; final manuscript received December 1, 2016; published online January 30, 2017. Editor: Y. Lawrence Yao.

produced by shaker to excite the machines during operation. Tatar et al. [12] excited the spindle by using active magnetic bearing and measured the response by laser Doppler vibrometer (LDV) in one direction and inductive displacement sensors in two orthogonal directions. Moreover, Tatar and Gren [13] indicated that it is desirable to measure the vibration on the rotating tool as close to the flutes as possible and used laser vibrometer for milling tool vibration measurements during cutting. Rantatalo et al. [14] adopted magnetic excitation and inductive displacement measurements of the spindle response and studied the effect of the gyroscopic moment and the speed-dependent bearing stiffness on the system dynamics for different spindle speeds. Faassen et al. [15] and Albrecht et al. [16] impacted the rotating cylinder point by impulse hammer and measured the response by laser sensor. Based on this method, Cao et al. [17] measured the FRFs at the tool tip of a dummy tool without any flutes. In addition, Cheng et al. [18] creatively combined this method and RCSA to predict rotating tool point frequency response. Matsubara et al. [19] presented a noncontact excitation method for evaluating the dynamic stiffness of a rotating spindle and investigated the dynamic uncertainty and its effect on cutting stability. The noncontact methods can directly excite the structure and measure the response, but require expensive equipment with high precision and complicated experimental setups.

In the other way, Gagnol et al. [4,20,21] elaborated a dynamic model of a high-speed spindle–bearing system on the basis of rotor dynamics predictions and readjusted the model with respect to experimental modal identification. The new stability lobe diagrams were predicted by integrating the modeled speed-dependent spindle transfer function in the chatter vibration stability approach. Özsahin et al. [22] identified the spindle bearing dynamics for various spindle rotational speeds and cutting forces. And the tool point FRFs under operating conditions were determined using the identified speed-dependent bearing dynamics. Özşahin et al. [3] also proposed an inverse stability solution by using experimentally determined chatter frequency and corresponding axial depth of cut to identify tool point FRFs. However, it is more challenging to determine depth of cut at the stability boundary accurately.

In this paper, a new identification method without using noncontact sensor is proposed for tool point FRFs identification under spindle rotating state. In this method, the cross FRFs with impact applied on smooth rotating tool and vibration response tested on spindle head are measured for two tools of different lengths clamped in spindle–holder assembly. An inverse receptance coupling substructure analysis (RCSA [23–26]) algorithm is developed to identify the FRFs of spindle–holder–partial tool assembly. Different from the purpose of reducing the experiment times when the combination of tool–holder is multiple in the previous RCSA researches, this paper developed the inverse RCSA to identify the tool point FRFs under spindle rotating state using the cross FRFs. An FEM simulation is performed to verify the validity of inverse RCSA algorithm. The tool point FRFs under various spindle rotational speeds are obtained by coupling the FRFs of the spindle–holder–partial tool and the other partial tool. The effect of the spindle rotating on the holder–tool dynamic behavior for different holder–tool stiffness is analyzed. Moreover, the effects of spindle rotational speed on tool point FRFs and stability lobe diagrams are investigated. And the stability diagrams calculated using the identified tool point FRFs under spindle rotating are verified with cutting experiment. The comparisons of spindle head–tool FRFs between spindle idle and rotating sate under different tool overhang length are analyzed.

2 Inverse RCSA Algorithm for Joint FRFs Identification

2.1 Inverse RCSA Algorithm. For the tool mounted on the rotating spindle, it is difficult to apply impact force on the tool point and measure the tool point vibration. However, the smooth part of the tool or the cylinder can be excited by impulse hammer [15,17], and the accelerometer can measure the vibration on the spindle head as close to the tool point as possible. The spindle head–tool smooth part FRF also contains the effect of spindle speed on spindle dynamic. Thus, under the spindle rotating state, it can obtain the tool point FRF by using the spindle head–tool smooth part FRF and RCSA.

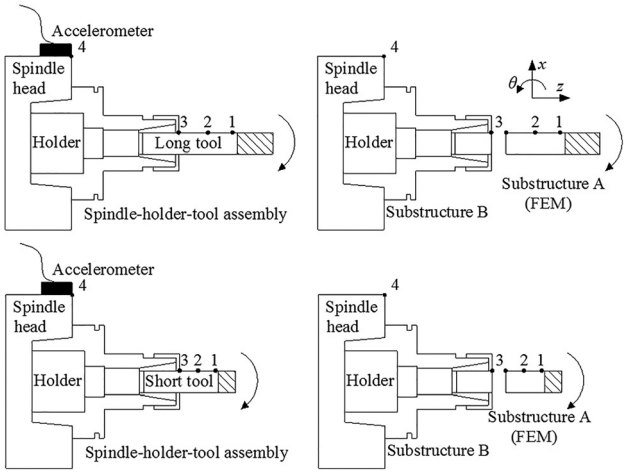

Fig. 1 Two tools of different lengths clamped in spindle–holder assembly and substructures

Two tools of different lengths clamped in spindle–holder assembly are adopted in this paper, as shown in Fig. 1. Point 1 and point 2 are located at the smooth part which can be impacted by impulse hammer under spindle rotating state. Point 4 is the nearest place to the tool point, and its vibration can be measured by the accelerometer. The spindle–holder–tool assembly is divided into two substructures: substructure A and substructure B as shown in Fig. 1. Point 3 is the rigid coupling point between substructures A and B.

For the spindle–holder–tool assembly, the displacement vector at point 4 can be expressed as

$$\begin{aligned}\mathbf{X}_{L,4} &= \mathbf{H}_{L,41}\mathbf{F}_{L,1} + \mathbf{H}_{L,42}\mathbf{F}_{L,2} + \mathbf{H}_{L,43}\mathbf{F}_{L,3} + \mathbf{H}_{L,44}\mathbf{F}_{L,4}\\ \mathbf{X}_{S,4} &= \mathbf{H}_{S,41}\mathbf{F}_{S,1} + \mathbf{H}_{S,42}\mathbf{F}_{S,2} + \mathbf{H}_{S,43}\mathbf{F}_{S,3} + \mathbf{H}_{S,44}\mathbf{F}_{S,4}\end{aligned} \tag{1}$$

where $\mathbf{X}$ is the displacement vector at point 4, and $\mathbf{F}$ is the force vector applied on the structure at points 1, 2, 3, and 4, respectively. The subscripts L and S denote the assembly with long and short tool, respectively. $\mathbf{H}_{L,ij}$ and $\mathbf{H}_{S,ij}$ vectors are FRFs between points i and j of the long and short tool assembly, respectively. It is important to note that the FRFs $\mathbf{H}_{L,ij}$ and $\mathbf{H}_{S,ij}$ vectors are the FRFs during spindle rotating, and the effect of the spindle rotating on dynamic behavior is contained in the FRFs $\mathbf{H}_{L,ij}$ and $\mathbf{H}_{S,ij}$.

Substructure A is the partial cutter without any constraint, the displacement vectors on substructure A at point 3 can be written as

$$\begin{aligned}\mathbf{X}_{LA,3} &= \mathbf{H}_{LA,31}\mathbf{F}_{L,1} + \mathbf{H}_{LA,32}\mathbf{F}_{L,2} + \mathbf{H}_{LA,33}\mathbf{F}_{LA,3}\\ \mathbf{X}_{SA,3} &= \mathbf{H}_{SA,31}\mathbf{F}_{S,1} + \mathbf{H}_{SA,32}\mathbf{F}_{S,2} + \mathbf{H}_{SA,33}\mathbf{F}_{SA,3}\end{aligned} \tag{2}$$

where the subscript A denotes substructure A.

Similarly, the displacement vectors on substructure B at point 3 and 4 are

$$\begin{bmatrix}\mathbf{X}_{LB,3}\\ \mathbf{X}_{LB,4}\end{bmatrix} = \begin{bmatrix}\mathbf{H}_{B,33} & \mathbf{H}_{B,34}\\ \mathbf{H}_{B,43} & \mathbf{H}_{B,44}\end{bmatrix}\begin{bmatrix}\mathbf{F}_{LB,3}\\ \mathbf{F}_{LB,4}\end{bmatrix}$$
$$\begin{bmatrix}\mathbf{X}_{SB,3}\\ \mathbf{X}_{SB,4}\end{bmatrix} = \begin{bmatrix}\mathbf{H}_{B,33} & \mathbf{H}_{B,34}\\ \mathbf{H}_{B,43} & \mathbf{H}_{B,44}\end{bmatrix}\begin{bmatrix}\mathbf{F}_{SB,3}\\ \mathbf{F}_{SB,4}\end{bmatrix} \tag{3}$$

where the subscript B denotes substructure B. The assemblies with long and short tool have the same substructure B, and the FRFs vectors $\mathbf{H}_{B,ij}$ are applicable to the two spindle–holder–tool assembly.

The equilibrium and compatibility conditions at the substructure A–B joint (point 3) provide the following boundary equations:

$$\begin{aligned}\mathbf{X}_{L,3} &= \mathbf{X}_{LA,3} = \mathbf{X}_{LB,3}\\ \mathbf{X}_{S,3} &= \mathbf{X}_{SA,3} = \mathbf{X}_{SB,3}\\ \mathbf{F}_{L,3} &= \mathbf{F}_{LA,3} + \mathbf{F}_{LB,3}\\ \mathbf{F}_{S,3} &= \mathbf{F}_{SA,3} + \mathbf{F}_{SB,3}\end{aligned} \tag{4}$$

which are used in coupling substructures A and B. By considering the compatibility and equilibrium equations in Eq. (4) in displacement vector expression of the spindle–holder–tool assembly and substructures A and B (Eqs. (2) and (3)), the displacement $\mathbf{X}$ can be expressed as a function of FRFs and applied forces on point 1, 2, 3, and 4 as follows:

$$\begin{aligned}\mathbf{X}_{L,4} &= \mathbf{H}_{B,43}(\mathbf{H}_{LA,33} + \mathbf{H}_{B,33})^{-1}\mathbf{H}_{LA,31}\mathbf{F}_{L,1} + \mathbf{H}_{B,43}(\mathbf{H}_{LA,33} + \mathbf{H}_{B,33})^{-1}\mathbf{H}_{LA,32}\mathbf{F}_{L,2}\\ &\quad + \mathbf{H}_{B,43}(\mathbf{H}_{LA,33} + \mathbf{H}_{B,33})^{-1}\mathbf{H}_{LA,33}\mathbf{F}_{L,3} + [\mathbf{H}_{B,44} - \mathbf{H}_{B,43}(\mathbf{H}_{LA,33} + \mathbf{H}_{B,33})^{-1}\mathbf{H}_{B,34}]\mathbf{F}_{L,4}\\ \mathbf{X}_{S,4} &= \mathbf{H}_{B,43}(\mathbf{H}_{SA,33} + \mathbf{H}_{B,33})^{-1}\mathbf{H}_{SA,31}\mathbf{F}_{S,1} + \mathbf{H}_{B,43}(\mathbf{H}_{SA,33} + \mathbf{H}_{B,33})^{-1}\mathbf{H}_{SA,32}\mathbf{F}_{S,2}\\ &\quad + \mathbf{H}_{B,43}(\mathbf{H}_{SA,33} + \mathbf{H}_{B,33})^{-1}\mathbf{H}_{SA,33}\mathbf{F}_{S,3} + [\mathbf{H}_{B,44} - \mathbf{H}_{B,43}(\mathbf{H}_{SA,33} + \mathbf{H}_{B,33})^{-1}\mathbf{H}_{B,34}]\mathbf{F}_{S,4}\end{aligned} \tag{5}$$

According to Eqs. (1) and (5), we can obtain the spindle–holder–tool assembly FRFs expressed by substructures A and B FRFs

$$\begin{cases}\mathbf{H}_{L,41} = \mathbf{H}_{B,43}(\mathbf{H}_{LA,33} + \mathbf{H}_{B,33})^{-1}\mathbf{H}_{LA,31}\\ \mathbf{H}_{L,42} = \mathbf{H}_{B,43}(\mathbf{H}_{LA,33} + \mathbf{H}_{B,33})^{-1}\mathbf{H}_{LA,32}\\ \mathbf{H}_{L,44} = \mathbf{H}_{B,44} - \mathbf{H}_{B,43}(\mathbf{H}_{LA,33} + \mathbf{H}_{B,33})^{-1}\mathbf{H}_{B,34}\end{cases}\\ \begin{cases}\mathbf{H}_{S,41} = \mathbf{H}_{B,43}(\mathbf{H}_{SA,33} + \mathbf{H}_{B,33})^{-1}\mathbf{H}_{SA,31}\\ \mathbf{H}_{S,42} = \mathbf{H}_{B,43}(\mathbf{H}_{SA,33} + \mathbf{H}_{B,33})^{-1}\mathbf{H}_{SA,32}\\ \mathbf{H}_{S,44} = \mathbf{H}_{B,44} - \mathbf{H}_{B,43}(\mathbf{H}_{SA,33} + \mathbf{H}_{B,33})^{-1}\mathbf{H}_{B,34}\end{cases} \tag{6}$$

In this paper, the translational and rotational degrees of the spindle–holder–tool assembly and substructures A and B at points 1, 2, 3, and 4 are shown in Fig. 1. Each FRF contains both translation and rotational displacement elements, hence the FRFs in Eq. (6) are expanded as

$$\mathbf{H}_{P,ij} = \begin{bmatrix} h_{P,ij,ff} & h_{P,ij,fM} \\ h_{P,ij,Mf} & h_{P,ij,MM}\end{bmatrix} \quad (P = L, \mathrm{LA}, S, \mathrm{SA}, B \quad i,j = 1,2,3,4) \tag{7}$$

where the subscript ff denotes the translation displacement caused by the force, and the subscript MM denotes the rotational displacement caused by the moment. Furthermore, according to reciprocity, we have $h_{P,ij,Mf} = h_{P,ji,fM}$.

As mentioned above, the spindle–holder–tool assembly FRFs $h_{L,41,ff}$, $h_{L,42,ff}$, $h_{L,44,ff}$, $h_{S,41,ff}$, $h_{S,42,ff}$, and $h_{S,44,ff}$ can be measured by impact experiment under spindle rotating state, and we can use those FRFs as the known values and obtain the following form by substituting Eq. (7) into Eq. (6):

$$\begin{cases} h_{L,41,ff} = \dfrac{h_{LA,31,ff}(h_{B,43,ff}h_{LB,33,MM} - h_{B,43,fM}h_{LB,33,fM}) + h_{LA,31,Mf}(h_{B,43,fM}h_{LB,33,ff} - h_{B,43,ff}h_{LB,33,fM})}{h_{LB,33,ff}h_{LB,33,MM} - h_{LB,33,fM}^2}\\ h_{L,42,ff} = \dfrac{h_{LA,32,ff}(h_{B,43,ff}h_{LB,33,MM} - h_{B,43,fM}h_{LB,33,fM}) + h_{LA,32,Mf}(h_{B,43,fM}h_{LB,33,ff} - h_{B,43,ff}h_{LB,33,fM})}{h_{LB,33,ff}h_{LB,33,MM} - h_{LB,33,fM}^2}\\ h_{L,44,ff} = h_{B,44,ff} - \dfrac{h_{B,43,ff}(h_{B,43,ff}h_{LB,33,MM} - h_{B,43,fM}h_{LB,33,fM}) + h_{B,43,fM}(h_{B,43,fM}h_{LB,33,ff} - h_{B,43,ff}h_{LB,33,fM})}{h_{LB,33,ff}h_{LB,33,MM} - h_{LB,33,fM}^2}\end{cases}\\ \begin{cases} h_{S,41,ff} = \dfrac{h_{SA,31,ff}(h_{B,43,ff}h_{SB,33,MM} - h_{B,43,fM}h_{SB,33,fM}) + h_{SA,31,Mf}(h_{B,43,fM}h_{SB,33,ff} - h_{B,43,ff}h_{SB,33,fM})}{h_{SB,33,ff}h_{SB,33,MM} - h_{SB,33,fM}^2}\\ h_{S,42,ff} = \dfrac{h_{SA,32,ff}(h_{B,43,ff}h_{SB,33,MM} - h_{B,43,fM}h_{SB,33,fM}) + h_{SA,32,Mf}(h_{B,43,fM}h_{SB,33,ff} - h_{B,43,ff}h_{SB,33,fM})}{h_{SB,33,ff}h_{SB,33,MM} - h_{SB,33,fM}^2}\\ h_{S,44,ff} = h_{B,44,ff} - \dfrac{h_{B,43,ff}(h_{B,43,ff}h_{SB,33,MM} - h_{B,43,fM}h_{SB,33,fM}) + h_{B,43,fM}(h_{B,43,fM}h_{SB,33,ff} - h_{B,43,ff}h_{SB,33,fM})}{h_{SB,33,ff}h_{SB,33,MM} - h_{SB,33,fM}^2}\end{cases} \tag{8}$$

where

$$\begin{aligned} h_{LB,33,uv} &= h_{LA,33,uv} + h_{B,33,uv}\\ h_{SB,33,uv} &= h_{SA,33,uv} + h_{B,33,uv} \quad (u,v = f,M)\end{aligned} \tag{9}$$

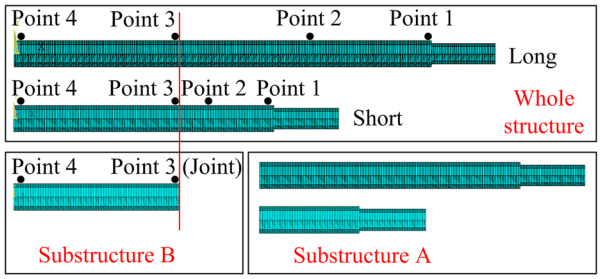

Fig. 2 FEM models

The FRFs of substructure A can be evaluated from the analytical method or the finite-element model of the beam, and the elements $h_{P,ij,uv}(P = \mathrm{LA}, \mathrm{SA} \quad i,j = 1,2,3,4 \quad u,v = f,M)$ in substructure A can be evaluated using a predetermined damping ratio for the tool material. To identify the tool point FRFs, we need to evaluate the FRF values at the joint $h_{B,33,ff}$, $h_{B,33,fM}$, and $h_{B,33,MM}$ [23]. Besides the FRFs of substructure A, Eq. (8) has six unknown FRFs $h_{B,33,ff}$, $h_{B,33,fM}$, $h_{B,33,MM}$, $h_{B,43,ff}$, $h_{B,43,fM}$, and $h_{B,44,ff}$. Equation (8) can be rewritten as

$$\begin{cases} h_{L,41,ff} = h_{LA,31,ff}G_{L1} + h_{LA,31,Mf}G_{L2} & (10a) \\ h_{L,42,ff} = h_{LA,32,ff}G_{L1} + h_{LA,32,Mf}G_{L2} & (10b) \\ h_{B,44,ff} - h_{L,44,ff} = h_{B,43,ff}G_{L1} + h_{B,43,fM}G_{L2} & (10c) \end{cases} \quad (10)$$

$$\begin{cases} h_{S,41,ff} = h_{SA,31,ff}G_{S1} + h_{SA,31,Mf}G_{S2} & (10d) \\ h_{S,42,ff} = h_{SA,32,ff}G_{S1} + h_{SA,32,Mf}G_{S2} & (10e) \\ h_{B,44,ff} - h_{S,44,ff} = h_{B,43,ff}G_{S1} + h_{B,43,fM}G_{S2} & (10f) \end{cases}$$

where

$$G_{L1} = \frac{(h_{B,43,ff}h_{LB,33,MM} - h_{B,43,fM}h_{LB,33,fM})}{h_{LB,33,ff}h_{LB,33,MM} - h_{LB,33,fM}^2}$$

$$G_{L2} = \frac{(h_{B,43,fM}h_{LB,33,ff} - h_{B,43,ff}h_{LB,33,fM})}{h_{LB,33,ff}h_{LB,33,MM} - h_{LB,33,fM}^2} \quad (11)$$

$$G_{S1} = \frac{(h_{B,43,ff}h_{SB,33,MM} - h_{B,43,fM}h_{SB,33,fM})}{h_{SB,33,ff}h_{SB,33,MM} - h_{SB,33,fM}^2}$$

$$G_{S2} = \frac{(h_{B,43,fM}h_{SB,33,ff} - h_{B,43,ff}h_{SB,33,fM})}{h_{SB,33,ff}h_{SB,33,MM} - h_{SB,33,fM}^2}$$

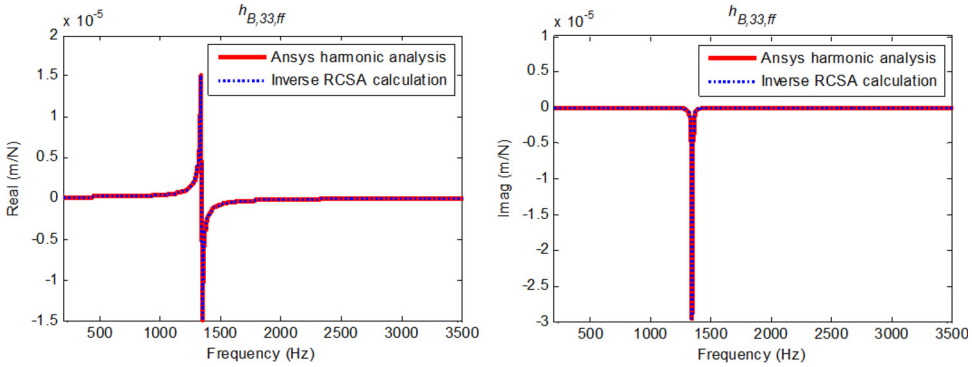

(*a*)

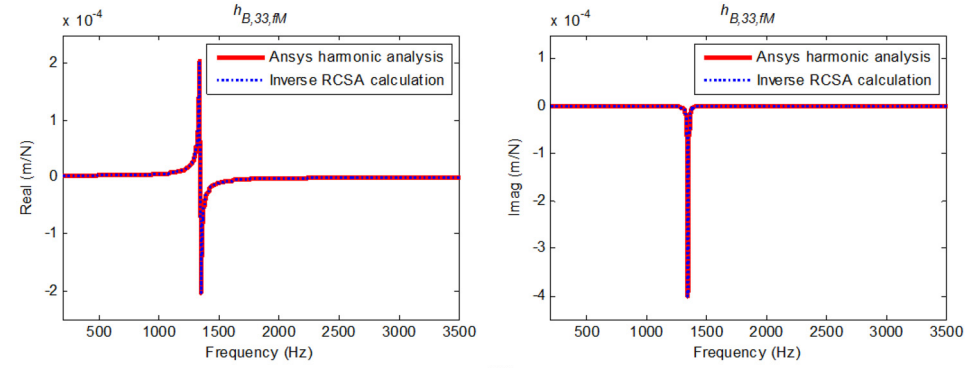

(*b*)

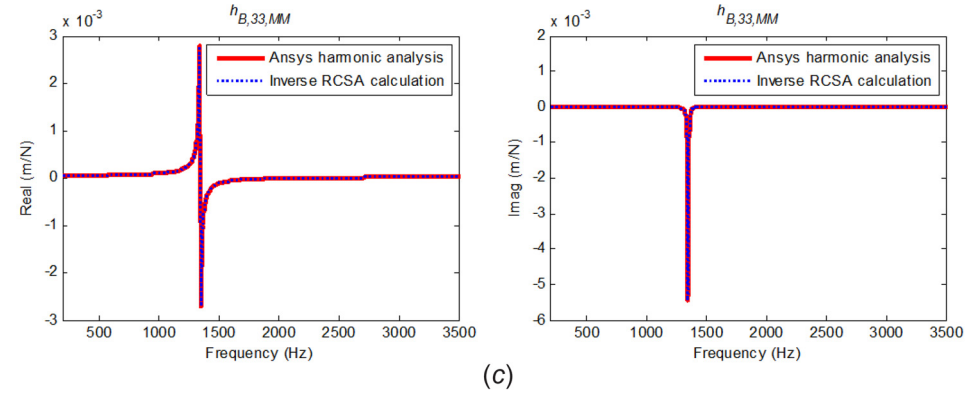

(*c*)

Fig. 3 FRFs obtained by ANSYS harmonic analysis and inverse RCSA calculation

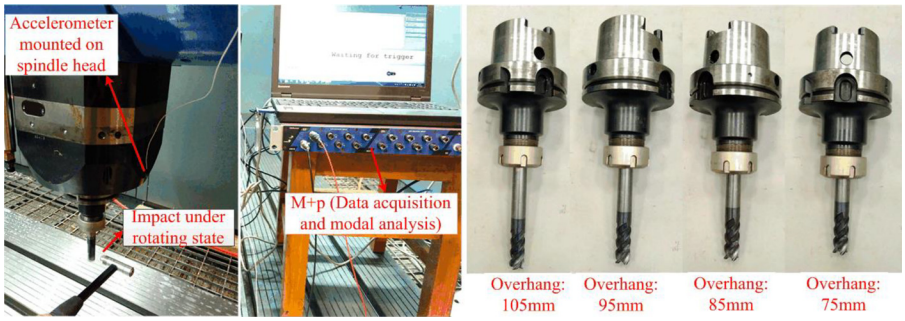

Fig. 4 Impact testing for different tool overhang

G_{L1} and G_{L2} can be calculated by solving Eqs. (10*a*) and (10*b*), and similarly for G_{S1} and G_{S2}. Then, in order to directly solve $h_{B,43,ff}$ and $h_{B,43,fM}$ according to Eqs. (10*c*) and (10*f*), the unknown $h_{B,44,ff}$ is also measured by impact experiment. It should be noted that the FRF $h_{B,44,ff}$ is measured with substructure B containing part of the tool. Thus, the equation only includes the three requested FRFs $h_{B,33,ff}$, $h_{B,33,fM}$, and $h_{B,33,MM}$, which can be obtained as

$$\begin{aligned} \frac{r(c+\delta)-s(b+\beta)}{(a+\kappa)(c+\delta)-(b+\beta)^2} &= G_{L1} \\ \frac{s(a+\kappa)-r(b+\beta)}{(a+\kappa)(c+\delta)-(b+\beta)^2} &= G_{L2} \\ \frac{r^2(g+\delta)-2rs(e+\beta)+s^2(d+\kappa)}{(d+\kappa)(g+\delta)-(e+\beta)^2} &= Z \end{aligned} \tag{12}$$

where $h_{B,44,ff}-h_{S,44,ff}=Z$, $h_{B,33,ff}=\kappa$, $h_{B,33,fM}=\beta$, $h_{B,33,MM}=\delta$, $h_{B,43,ff}=r$, $h_{B,43,fM}=s$, $h_{LA,33,ff}=a$, $h_{LA,33,fM}=b$, $h_{LA,33,MM}=c$, $h_{SA,33,ff}=d$, $h_{SA,33,fM}=e$, and $h_{SA,33,MM}=g$.

Three unknown parameters κ, β, and δ can be got through solving Eq. (12). Finally, the tool point FRFs are identified by κ, β, δ, and FRFs of substructure A using two-component RCSA [23].

The typical RCSA method uses only one cylinder or tool to identify the joint parameters $h_{B,33,ff}$, $h_{B,33,fM}$, and $h_{B,33,MM}$ under the idle state. However, under spindle rotating state, the accelerometer can only be mounted on the spindle head which is not rotating, which produces more unknown FRFs in RCSA equation. Thus, this paper adopts two tools of different lengths (or cylinder) and develops the inverse RCSA algorithm to identify the joint parameters.

2.2 FEM Simulation Verification. In this section, FEM simulation verification for the inverse RCSA algorithm is provided. The ANSYS models of two structures of different lengths are shown in Fig. 2. All the FRFs of the ANSYS models can be obtained by harmonic analysis. The centrifugal force produced by rotating state will result in prestress in the structures, and the prestress analysis with applied angular velocity is performed before the harmonic analysis.

According to the model in Fig. 1, points 3 and 4 are assumed to be as the joint point and point on spindle head, respectively. Points 1 and 2 are the excitation points on the smooth part of tool. Since the response on point 4 in Fig. 1 can be obtained by impact experiment. Thus, the FRFs $h_{L,41,ff}$, $h_{L,42,ff}$, $h_{L,44,ff}$, $h_{S,41,ff}$, $h_{S,42,ff}$, $h_{S,44,ff}$, and $h_{B,44,ff}$ in Fig. 2 are the known parameters. Besides, substructure A in Fig. 1 can be modeled and analyzed by ANSYS, and thus, all the FRFs of substructure A in Fig. 2 can be realized as the known values. The required FRFs on joint (point 3) of substructure B $h_{B,33,ff}$, $h_{B,33,fM}$, and $h_{B,33,MM}$ in Fig. 2 are realized as the unknown values and should be calculated by the known values and inverse RCSA algorithm. Finally, the FRFs on joint (point 3) of substructure B identified by the proposed inverse RCSA algorithm are compared to that by direct ANSYS harmonic analysis.

As seen from Fig. 3, the joint FRFs identified by the proposed inverse RCSA are compared with that analyzed by FEM which shows good agreement. Theoretically, the FEM simulation demonstrates that the proposed inverse RCSA in this paper can accurately identify the joint FRFs with the condition when only the spindle head response can be measured.

3 Experimental Identification

The proposed inverse RCSA algorithm has been confirmed by the FEM simulation in theory. Further, proposed inverse RCSA algorithm is applied on a machining-center GMC 1600H/2. In this section, first, the effect of the spindle rotating on the holder–tool dynamic behavior for different holder–tool stiffness is analyzed. Second, variation of the tool point FRF due to the spindle rotating state is tested.

3.1 The Effect of the Spindle Rotating on the Holder–Tool Dynamic Behavior. During the actual cutting operations, the tool overhang is adjusted according to the cutting condition requirement, however, the tool overhang change leads to the holder–tool combination dynamic behavior variation. Thus, this study investigates the effect of the spindle rotating on the holder–tool dynamic behavior for different holder–tool stiffness by introducing different tool overhang. The holder and tool used in experiment are HSK A100 and four-fluted helical mill cutter with length 116 mm, respectively. The spindle head–tool FRFs with different tool overhang are obtained by the impact testing. Figure 4 shows the model impact test under spindle rotating state on the machining-center GMC 1600H/2. It can be seen that the accelerometer is mounted on the spindle head where it is closer to the tool point and not rotating. The vibration signal on spindle head is acquired by a DYTRAN acceleration sensor 3224A1, and the exciting force on the smooth part of the tool is applied by a PCB impulse hammer 086C03. M+p (VibRunner hardware and SMARTOFFICE software) is used for data acquisition and modal analysis. Referring to the impact method performed by Faassen et al. [15] and Cao et al. [17], the impulse hammer is impacting on the smooth part of the tool. The modal impact testing is conducted ten times in each direction, and the FRF is averaged to reduce the impact uncertainty.

Figure 5 gives the comparison of the FRFs with different tool overhang under the idle state and spindle speed 5000 rpm state. As shown in Fig. 5, it can be seen that the discrepancy appears until the tool overhang shortening to 75 mm in x direction, however, the FRFs in y direction have no discrepancy only on the condition of the tool overhang 105 mm.

Özşahin et al. [3] indicated that for the cases where tool mode is dominant, the tool point FRFs are not affected by rotating speeds. However, when the spindle mode is dominant, the tool point FRFs show a speed-dependent behavior. For this study, the effect of the spindle rotating state on holder–tool dynamic

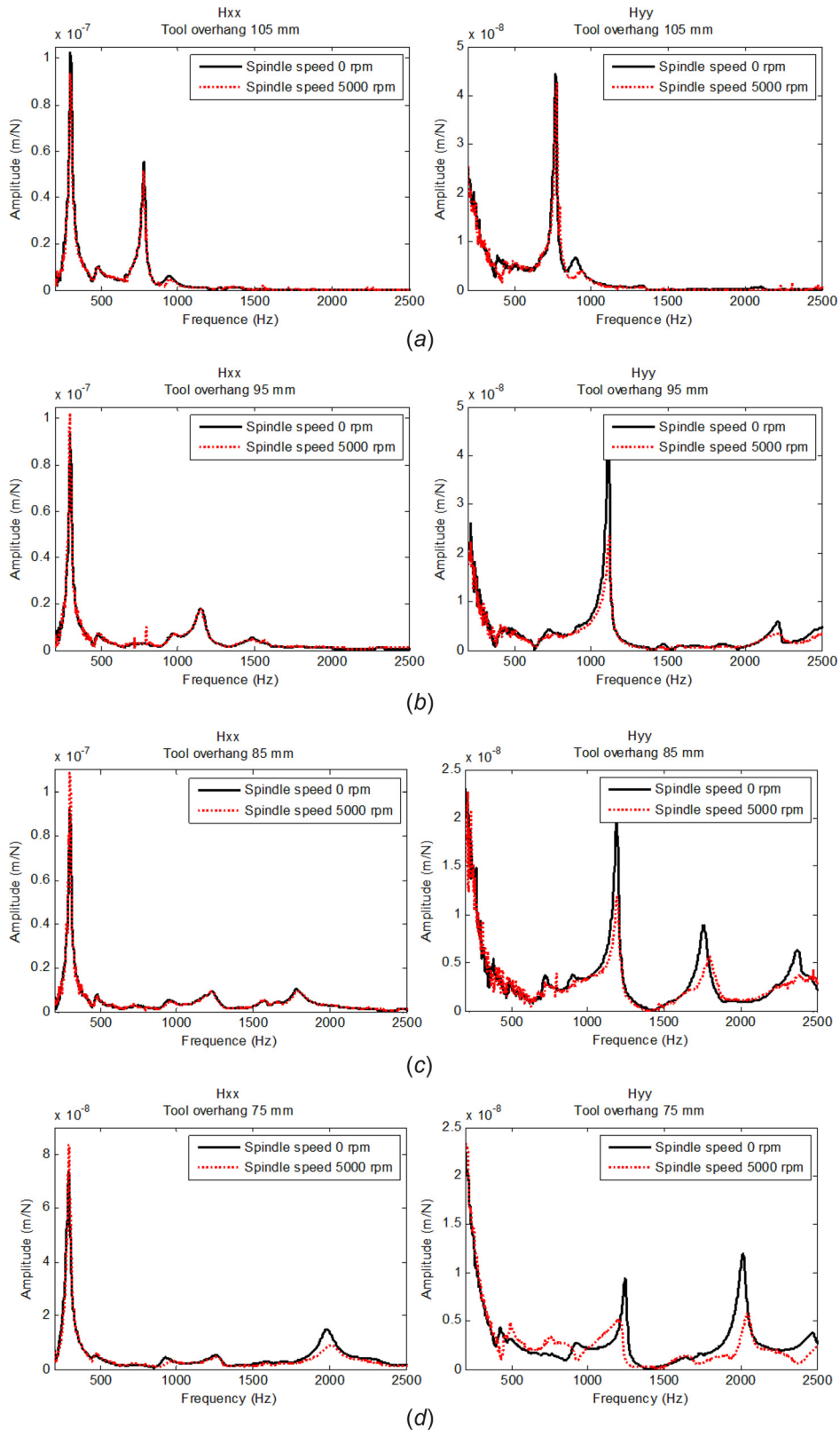

Fig. 5 Comparison of FRF measured under different tool overhang: (*a*) tool overhang length is 105 mm, (*b*) tool overhang length is 95 mm, (*c*) tool overhang length is 85 mm, and (*d*) tool overhang length is 75 mm

behavior depends on the stiffness of the holder–tool assembly. When the long tool overhang results in the poor stiffness of the holder–tool assembly, the magnitude of holder–tool mode (FRF) is much larger than the mode variation caused by the spindle rotating state. Therefore, the spindle rotating state has negligible influence on the holder–tool mode. However, when the holder–tool assembly has good stiffness with short tool overhang, the magnitude of holder–tool mode is comparable to the mode

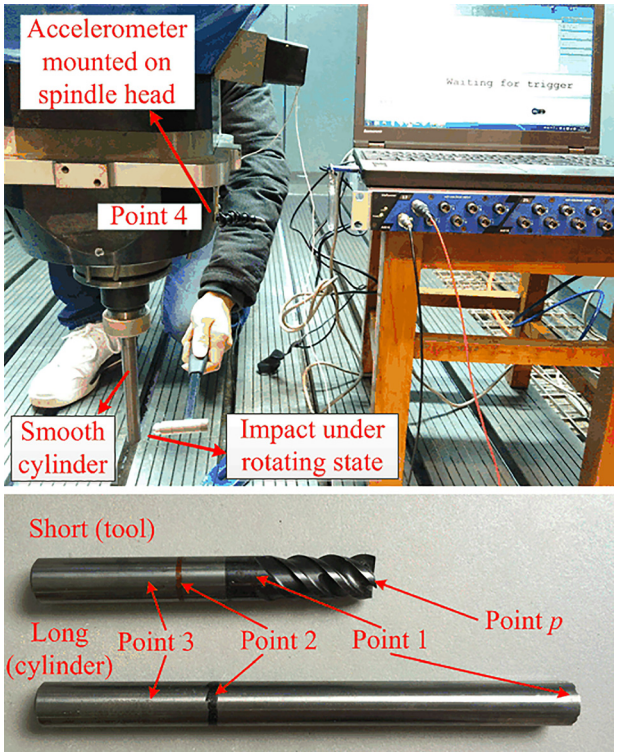

Fig. 6 Impact experiments under spindle rotating state

Table 1 Parameters of the cutter and cylinder

	Length (mm)	Diameter (mm)	Overhang length (mm)	Material
Cutter	116	16	75	Carbide alloy
Cylinder	186	16	145	Carbide alloy

variation caused by the spindle rotating state. And the influence of the spindle rotating state on holder–tool mode is obvious. In the practical machining, the stiffness of holder–tool is usually adopted as good as possible for avoiding vibration. Thus, the influence of the spindle rotating state should be considered in the stability prediction model for the actual machining.

3.2 Tool Point FRFs Identification Under Spindle Rotating State. Besides the four-fluted helical mill cutter, a longer smooth cylinder is used to meet the request of two tools of different lengths (or cylinder) in the proposed inverse RCSA algorithm. According to the inverse RCSA algorithm described above, the FRFs with response on spindle head should be measured by model impact test. Figure 6 shows the model impact test under spindle rotating state on the machining-center GMC 1600 H/2.

In this paper, the four-fluted helical mill cutter and the smooth cylinder are used as the short and long tools, respectively. The helix angle and flute length of the cutter are 50 deg and 42 mm, respectively. The parameters of the cutter and cylinder are listed in Table 1. As shown in Fig. 6, the impact points (points 1 and 2) are located on the smooth part of the cutter.

The spindle head–tool FRFs in the x and y directions are obtained by impact testing for different spindle speeds (0 rpm, 3000 rpm, 4000 rpm, and 5000 rpm) of the machining center, as shown in Fig. 7. As seen from Figs. 7(*a*)–7(*d*), it can be found that the first mode with natural frequency of 296 Hz appears in the FRFs of cutter and cylinder in the x direction, simultaneously. However, the second mode for the cylinder and cutter are 550 Hz and 1980 Hz, respectively. Thus, the second mode is the mode of the cutter and cylinder. Similarly, as seen from Figs. 7(*e*)–7(*h*), the mode of cylinder in the y direction is 544 Hz and 546 Hz, and the modes with 1244 Hz and 2014 Hz are the modes for cutter in the y direction. It is observed that the mode of cylinder and cutter shows a speed-dependent behavior.

As seen from Fig. 7, under different spindle speeds, obvious deviations are observed in the FRFs $h_{L,42,ff}$, $h_{S,41,ff}$, and $h_{S,42,ff}$, however, the deviations in the FRFs $h_{L,41,ff}$ are almost negligible. The holder–tool mode in FRFs $h_{L,41,ff}$ has larger amplitude than that in the other FRFs. According to the analysis in Sec. 3.1, the holder–tool mode in FRFs $h_{L,41,ff}$ is affected by the spindle rotating negligibly.

According to the identification method proposed by this paper, the joint FRFs $h_{B,33,ff}$, $h_{B,33,fM}$, and $h_{B,33,MM}$ can be identified by using the FRFs of the cutter and cylinder obtained by impact testing in Fig. 7 and FEM. Then, the tool point FRFs are calculated by the RCSA method in Ref. [25]. Since the model testing can be performed on the tool point under idle state, the tool point FRFs of the four-fluted helical mill cutter with overhang length 75 mm and 70 mm are used for verifying the accuracy of the identified joint FRFs $h_{B,33,ff}$, $h_{B,33,fM}$, and $h_{B,33,MM}$. Figure 8 shows the comparison of tool point FRF in the x and y directions obtained by impact testing with that identified by the proposed method. It can be seen that the identified FRFs are in good agreement with the tested FRFs. On the base of the FEM simulation verification in Sec. 2.2, the proposed method, which can identify the tool point FRFs using the FRFs with only the spindle head response, is also demonstrated by the impact testing under idle state.

The FRFs obtained for the different spindle rotating speeds with the tool overhang length 75 mm are presented in Fig. 9. From these results, it is obvious that the amplitude and frequency of the tool point FRF under spindle speed 3000 rpm have a significant decrease and shift compared with that under spindle idle state. Then, the tool point FRF has a further variation with the spindle speed increasing. The discrepancies of the tool point FRF between spindle speed 3000 rpm, 4000 rpm, and 5000 rpm are not as significant as that between spindle speed 3000 rpm and idle state. Consequently, the influence of spindle state on the tool point FRF can be summarized in two aspects: one is the spindle rotating state (rotating or not), and the other is the spindle rotating speed. It is known that at high speeds, gyroscopic moments and centrifugal forces and bearing stiffnesses cause variations of the spindle modes [27]. In addition, the structural variation under spindle rotating, such as drive chain change, etc., also affects the mode. For the machining-center GMC 1600 H/2 used in this study, the tool mode variation caused by the spindle rotating state (rotating or not) is regarded as the result from the structural variation. And the tool mode variation caused by the spindle speed is regarded as the result from the gyroscopic moments and centrifugal forces, bearing stiffnesses variation, etc. Modal parameter data can be extracted from the identified FRF and are listed in Table 2.

4 Stability Experiment for Identified FRFs Verification and Analysis

In order to verify the accuracy of the identified tool point FRFs under spindle rotating state, stability prediction and cutting experiments are performed on the machining-center GMC 1600 H/2 with the four-fluted helical mill cutter, as shown in Fig. 10. Cutting is performed on 300 M steel workpiece with 25% radial immersion and 0.05 mm/tooth feed. The cutting force coefficients, $K_t = 3127$ MPa and $K_r = 1769$ MPa, are calibrated by experiment. During the experiment, a KISTLER 9257 A dynamometer and an NI PXIe-4499 data-acquisition module are used to record the force signals. The chatter stability limit is identified using the spectrum of the force information.

As seen in Fig. 9, the identified tool point FRFs under spindle rotating state show a speed-dependent behavior. Therefore, for different speeds, tool point FRFs should be identified at each spindle speed considered. And along the required speed range, the

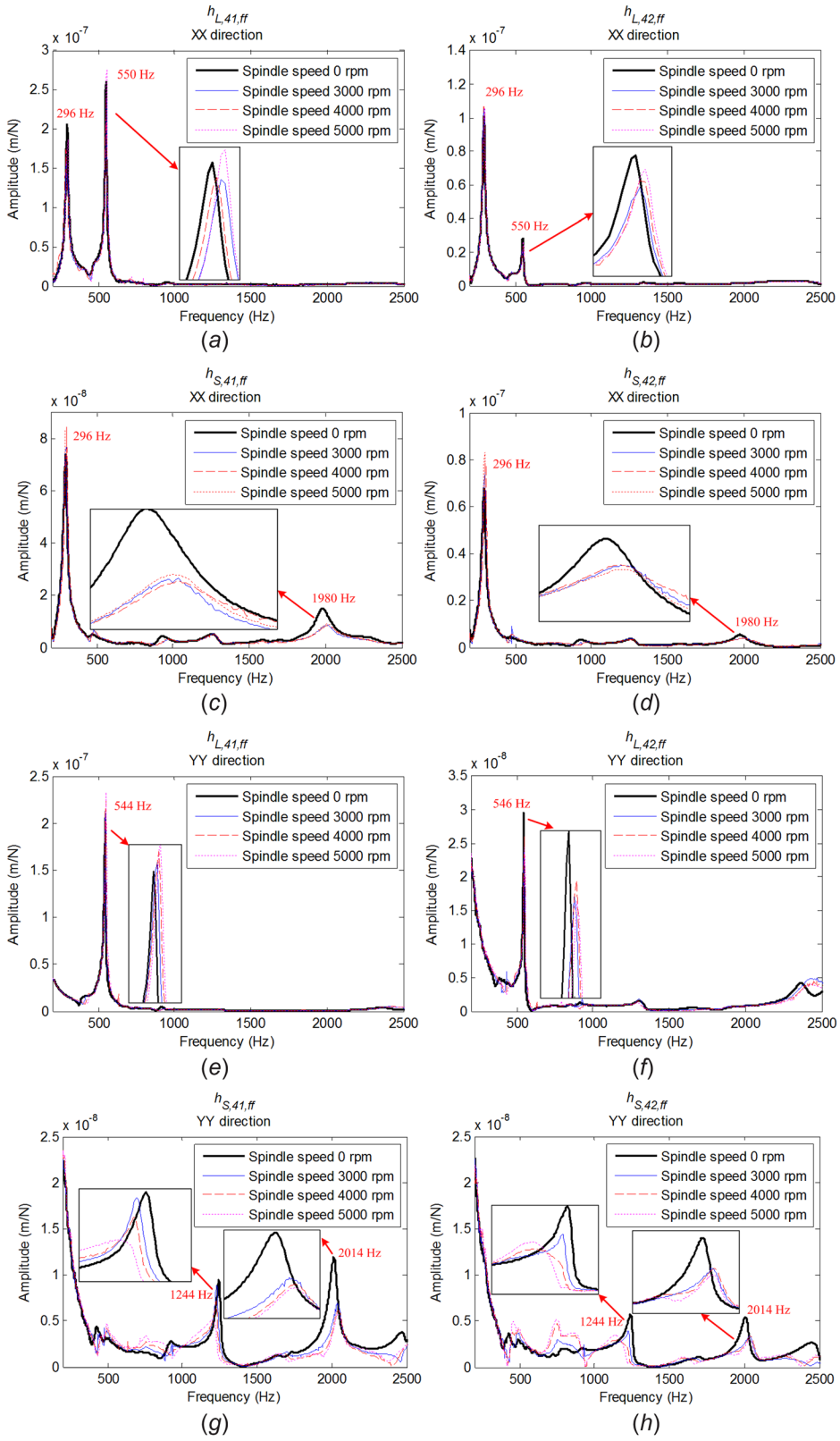

Fig. 7 FRFs tested by model impact

stability diagrams should be calculated for every speed. In order to avoid the process damping effect, the stability prediction uses the identified tool point FRFs under spindle speeds 4000 rpm and 5000 rpm.

Using the time-domain method [28] and the modal parameters listed in Table 2, the predicted stability diagrams under spindle speeds 4000 rpm and 5000 rpm are shown in Fig. 11. In addition, the stability diagrams for the idle state are also shown in Fig. 11. The stability diagrams using the identified tool point FRFs under spindle rotating state are called modified stability. In this study, it is noticed that the critical depth of cut of the stability boundary increases while considering the spindle rotating state effect.

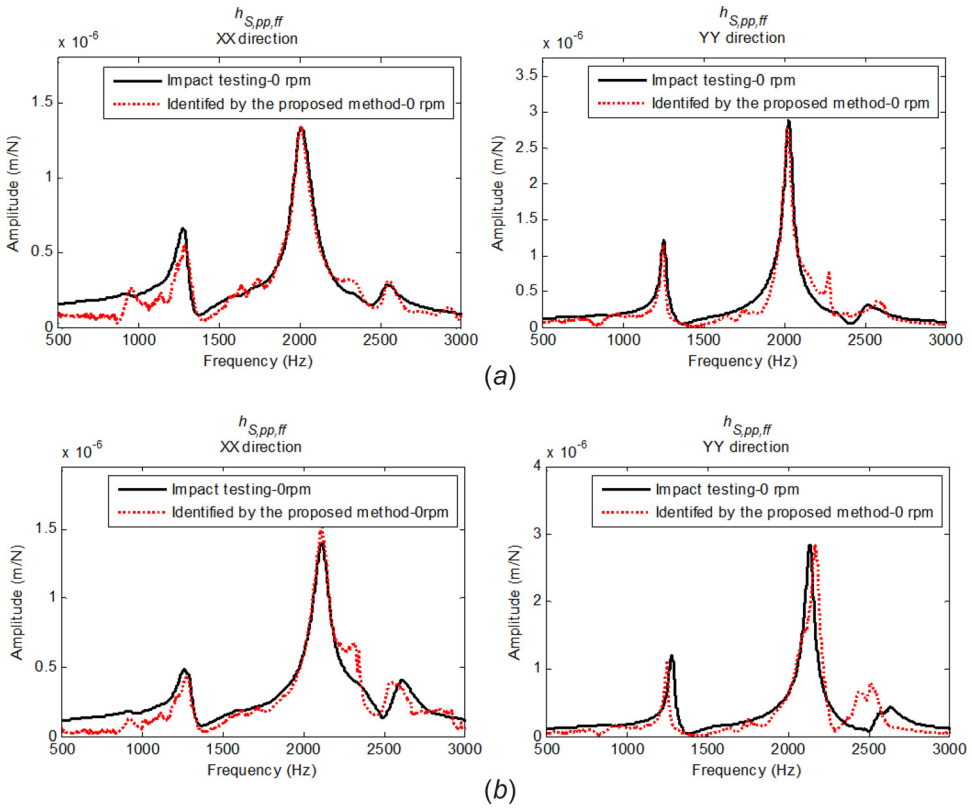

Fig. 8 Comparison of tool point FRF in *x* and *y* directions obtained using impact testing with that identified by the proposed method: (*a*) tool overhang length is 75 mm and (*b*) tool overhang length is 70 mm

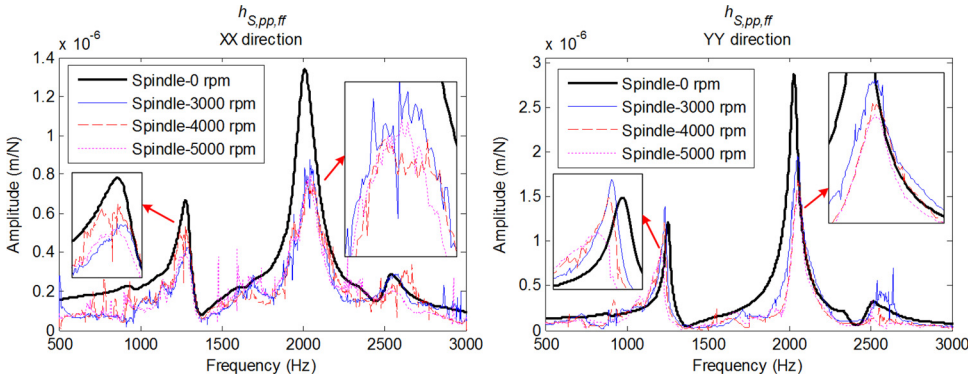

Fig. 9 Identified tool point FRFs under different spindle rotating speeds

Table 2 Comparison of the model parameters under different spindle rotating speeds

		Mode 1		Mode 2	
Spindle speed (rpm)		Natural frequency (Hz)	Damping (%)	Natural frequency (Hz)	Damping (%)
x–x	0	1282	2.6	2011	3.01
	3000	1292	2.01	2040	2.38
	4000	1272	2.05	2042	2.92
	5000	1284	2.2	2042	2.74
y–y	0	1255	1.22	2032	1.25
	3000	1232	1.34	2048	1.24
	4000	1212	1.59	2056	0.92
	5000	1183	2.78	2054	1.18

Fig. 10 Cutting experiment

In order to verify the stability boundary, the cutting experiments are performed with spindle speeds 4000 rpm and 5000 rpm. The cutting results are shown in Fig. 11, and the spectrum analysis of cutting forces F_x at some parameter points (A, B, C, and D) are shown in Fig. 12. The force spectrum in the x direction of point A (4000 rpm and 0.8 mm) has the chatter frequencies of 2076 Hz and 2343 Hz. On the other hand, point B (4000 rpm and 0.6 mm), only the harmonic vibration frequencies (1067 Hz, 1333 Hz, 1867 Hz, 2133 Hz, etc.) appear, where frequencies are integral multiples of the spindle speed frequency (4000/60 = 66.67 Hz). Point C (5000 rpm, 2.2 mm) is unstable due to the occurrence of chatter frequencies (1245 Hz, 2245 Hz, 2578, etc.). Point D (5000 rpm and 2.0 mm) is stable, and the corresponding frequencies (999.9 Hz, 1250 Hz, 1333 Hz, etc.) in the spectrum are all of the harmonic vibration frequencies.

For the cutting experiment with 4000 rpm, chatter occurred at 0.8 mm axial depth of cut. The predicted axial depth limit of cut using stability diagrams for spindle speed 4000 rpm and idle state is 0.65 mm and 0.3 mm, respectively. For the cutting experiment

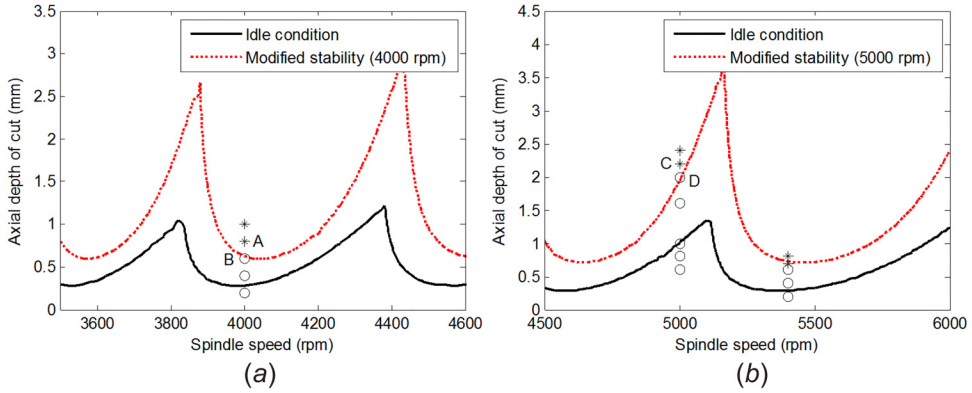

Fig. 11 (*a*) Stability diagrams obtained for idle state and 4000 rpm spindle speed and (*b*) stability diagrams obtained for idle state and 5000 rpm spindle speed. The symbols are follows: (1) ○ is a stable case and (2) * is an unstable cutting case.

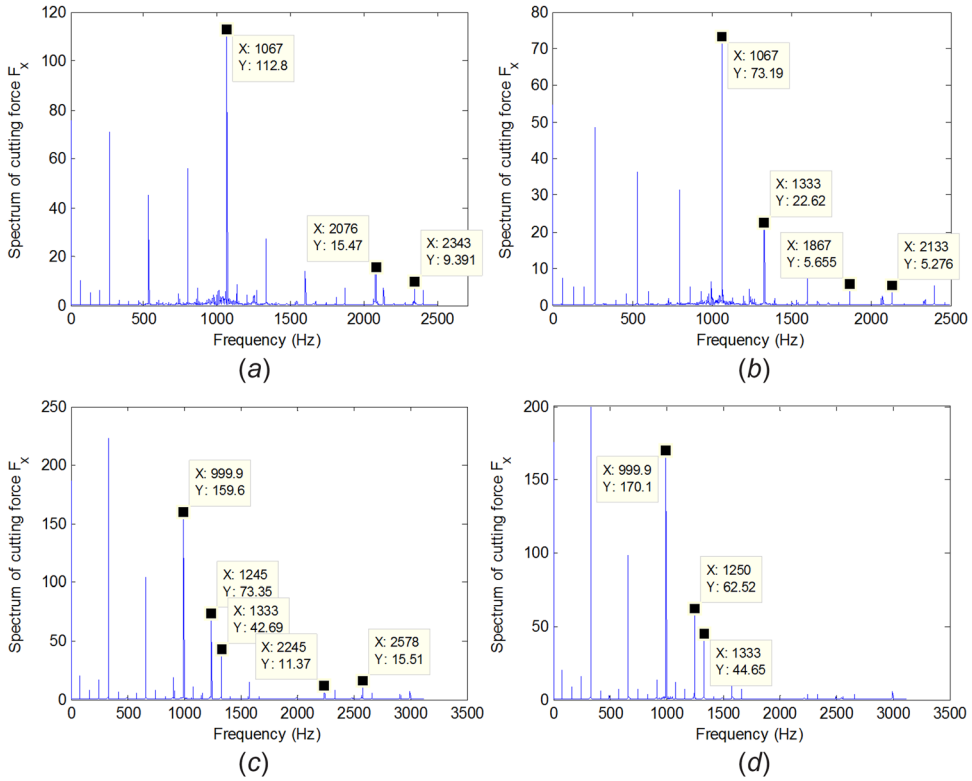

Fig. 12 Cutting force spectrum of F_x at different parameter points: (*a*) point A (chatter), (*b*) point B (stable), (*c*) point C (chatter), and (*d*) point D (stable)

with 5000 rpm, chatter occurred at 2.2 mm axial depth of cut. The predicted axial depth limit of cut using stability diagrams for spindle speed 5000 rpm and idle state is 1.95 mm and 1.0 mm, respectively. Thus, the modified stability diagrams provide more accurate chatter predictions compared with stability diagrams obtained using tool point FRFs at idle state.

Moreover, the cutting with 5400 rpm spindle speed is also performed to check the accuracy of the modified stability diagrams at spindle speed 5000 rpm, which are close to the actual cutting speed 5400 rpm. It can be seen in Fig. 11(*b*) that chatter occurred at 0.7 mm axial depth of cut with the predicted axial depth limit of cut 0.72 mm. Thus, it can be concluded that, compared with stability diagrams obtained using idle FRFs, the modified stability diagram provides many accurate stability predictions not only for the spindle speeds used in the FRFs identification but also for different spindle speeds close to the identification region.

5 Conclusions

In this paper, a new identification method is proposed for tool point FRFs identification under spindle rotating state. Since only the response on the spindle head can be measured by accelerometer under spindle rotating state, the cross FRFs with impact applied on smooth rotating tool and vibration response tested on spindle head are measured for two tools of different lengths clamped in spindle–holder assembly. And then, an inverse RCSA algorithm is developed to identify the FRFs of spindle–holder–partial tool assembly. The proposed inverse RCSA algorithm is verified by an FEM simulation and an experiment on the speed idle state. Using the FRFs of spindle–holder–partial tool assembly and the RCSA, the FRFs of the tool point under different spindle speeds are obtained. In addition, stability prediction and analysis during spindle rotating are performed.

The spindle head–tool FRFs test results show that the effect of the spindle rotating state on the holder–tool dynamic behavior depends on the stiffness of the holder–tool assembly. For the good stiffness of holder–tool adopted in practical machining, the influence of the spindle rotating state on the holder–tool mode is obvious and should be considered in the stability prediction for accurate machining parameters optimization. The stability lobe diagrams predicted by the identified tool point FRFs under spindle rotating state show that the spindle rotating improves the stability boundary.

In addition to the success of the proposed method in tool point FRF identification under spindle rotating state and more accurate stability prediction at high-speed machining, an important contribution of the proposed method is that requirements for expensive equipment, complicated experimental setups, and signal processing problem are eliminated. Moreover, the challenge to determine depth of the axial depth of cut at stability boundary accurately in the inverse stability solution method is avoided. The proposed method only requires the traditional impact testing on two different length cutters (or cylinder).

Acknowledgment

This work was partially supported by the National Natural Science Foundation of China under Grant No. 51275189, the Project of Key Technology Innovation Project of Hubei Province under Grant No. 2015AAA002, and the National Natural Science Foundation of China under Grant No. 51421062.

Reference

[1] Altintas, Y., and Budak, E., 1995, "Analytical Prediction of Stability Lobes in Milling," CIRP Ann. Manuf. Technol., **44**(1), pp. 357–362.
[2] Budak, E., and Altintas, Y., 1998, "Analytical Prediction of Chatter Stability in Milling—Part I: General Formulation," ASME J. Dyn. Syst. Meas. Control, **120**(1), pp. 22–30.
[3] Özşahin, O., Budak, E., and Özgüven, H. N., 2015, "In-Process Tool Point FRF Identification Under Operational Conditions Using Inverse Stability Solution," Int. J. Mach. Tools Manuf., **89**, pp. 64–73.
[4] Gagnol, V., Le, T. P., and Ray, P., 2011, "Modal Identification of Spindle-Tool Unit in High-Speed Machining," Mech. Syst. Signal Process., **25**(7), pp. 2388–2398.
[5] Shin, Y. C., 1992, "Bearing Nonlinearity and Stability Analysis in High Speed Machining," ASME J. Eng. Ind., **114**(1), pp. 23–30.
[6] Tounsi, N., and Otho, A., 2000, "Identification of Machine-Tool-Workpiece System Dynamics," Int. J. Mach. Tools Manuf., **40**(9), pp. 1367–1384.
[7] Özsahin, O., Budak, E., and Özgüven, H. N., 2011, "Investigating Dynamics of Machine Tool Spindles Under Operational Conditions," Adv. Mater. Res., **223**, pp. 610–621.
[8] Li, B., Cai, H., Mao, X., Huang, J., and Luo, B., 2013, "Estimation of CNC Machine-Tool Dynamic Parameters Based on Random Cutting Excitation Through Operational Modal Analysis," Int. J. Mach. Tools Manuf., **71**, pp. 26–40.
[9] Cai, H., Mao, X., Li, B., and Luo, B., 2015, "Estimation of FRFs of Machine Tools in Output-Only Modal Analysis," Int. J. Adv. Manuf. Technol., **77**(1–4), pp. 117–130.
[10] Zaghbani, I., and Songmene, V., 2009, "Estimation of Machine-Tool Dynamic Parameters During Machining Operation Through Operational Modal Analysis," Int. J. Mach. Tools Manuf., **49**(12–13), pp. 947–957.
[11] Mohanty, P., and Rixen, D. J., 2004, "Operational Modal Analysis in the Presence of Harmonic Excitation," J. Sound Vib., **270**(1–2), pp. 93–109.
[12] Tatar, K., Rantatalo, M., and Gren, P., 2007, "Laser Vibrometry Measurements of an Optically Smooth Rotating Spindle," Mech. Syst. Signal Process., **21**(4), pp. 1739–1745.
[13] Tatar, K., and Gren, P., 2008, "Measurement of Milling Tool Vibrations During Cutting Using Laser Vibrometry," Int. J. Mach. Tools Manuf., **48**(3–4), pp. 380–387.
[14] Rantatalo, M., Aidanpää, J. O., and Göransson, B. P., 2007, "Milling Machine Spindle Analysis Using FEM and Non-Contact Spindle Excitation and Response Measurement," Int. J. Mach. Tools Manuf., **47**(7–8), pp. 1034–1045.
[15] Faassen, R. P. H., Wouw, N., Oosterling, J. A. J., and Nijmeijer, H., 2003, "Prediction of Regenerative Chatter by Modelling and Analysis of High-Speed Milling," Int. J. Mach. Tools Manuf., **43**(14), pp. 1437–1446.
[16] Albrecht, A., Park, S. S., Altintas, Y., and Pritschow, G., 2005, "High Frequency Bandwidth Cutting Force Measurement in Milling Using Capacitance Displacement Sensors," Int. J. Mach. Tools Manuf., **45**(9), pp. 993–1008.
[17] Cao, H., Li, B., and He, Z., 2012, "Chatter Stability of Milling With Speed-Varying Dynamics of Spindles," Int. J. Mach. Tools Manuf., **52**(1), pp. 50–58.
[18] Cheng, C. H., Schmitz, T. L., and Duncan, G. S., 2007, "Rotating Tool Point Frequency Response Prediction Using RCSA," Mach. Sci. Technol., **11**(3), pp. 433–446.
[19] Matsubara, A., Tsujimoto, S., and Kono, D., 2015, "Evaluation of Dynamic Stiffness of Machine Tool Spindle by Non-Contact Excitation Tests," CIRP Ann. Manuf. Technol., **64**(1), pp. 365–368.
[20] Gagnol, V., Bouzgarrou, B. C., Ray, P., and Barra, C., 2007, "Model-Based Chatter Stability Prediction for High-Speed Spindles," Int. J. Mach. Tools Manuf., **47**(7–8), pp. 1176–1186.
[21] Gagnol, V., Bouzgarrou, B. C., Ray, P., and Barra, C., 2007, "Stability-Based Spindle Design Optimization," ASME J. Manuf. Sci. Eng., **129**(1), pp. 407–415.
[22] Özşahin, O., Budak, E., and Özgüven, H. N., 2015, "Identification of Bearing Dynamics Under Operational Conditions for Chatter Stability Prediction in High Speed Machining Operations," Precis. Eng., **42**, pp. 53–65.
[23] Schmitz, T. L., 2000, "Predicting High-Speed Machining Dynamics by Substructure Analysis," CIRP Ann. Manuf. Technol., **49**(1), pp. 303–308.
[24] Schmitz, T. L., Davies, M. A., and Kennedy, M. D., 2001, "Tool Point Frequency Response Prediction for High-Speed Machining by RCSA," ASME J. Manuf. Sci. Eng., **123**, pp. 700–707.
[25] Park, S. S., Altintas, Y., and Movahhedy, M., 2003, "Receptance Coupling for End Mills," Int. J. Mach. Tools Manuf., **43**(9), pp. 889–896.
[26] Mancisidor, I., Urkiola, A., Barcena, R., Munoa, J., Dombovari, Z., and Zatarain, M., 2014, "Receptance Coupling for Tool Point Dynamic Prediction by Fixed Boundaries Approach," Int. J. Mach. Tools Manuf., **78**, pp. 18–29.
[27] Ertürk, A., Özgüven, H. N., and Budak, E., 2007, "Effect Analysis of Bearing and Interface Dynamics on Tool Point FRF for Chatter Stability in Machine Tools by Using a New Analytical Model for Spindle-Tool Assemblies," Int. J. Mach. Tools Manuf., **47**(1), pp. 23–32.
[28] Tang, X., Peng, F., Yan, R., Gong, Y., Li, Y., and Jiang, L., 2016, "Accurate and Efficient Prediction of Milling Stability With Updated Full-Discretization Method," Int. J. Adv. Manuf. Technol. (online).